Hindawi
Structural Control and Health Monitoring
Volume 2023, Article ID 1429761, 13 pages
https://doi.org/10.1155/2023/1429761

Research Article

Two Dimensional Finite Difference Model with a Singularity Attenuation Factor for Structural Health Monitoring of Single Lap Joints

Francesco Nicassio,[1] **Pierandrea Vergallo**,[2,3] **Raffaele Vitolo**,[3,4] **and Gennaro Scarselli**[1]

[1]*Department of Engineering for Innovation, University of Salento, Lecce, Italy*
[2]*Department of Mathematical, Computer, Physical and Earth Sciences, University of Messina, Messina, Italy*
[3]*Section of Lecce, INFN, Lecce, Italy*
[4]*Department of Mathematics and Physics "E. De Giorgi", University of Salento, Lecce, Italy*

Correspondence should be addressed to Gennaro Scarselli; gennaro.scarselli@unisalento.it

Received 7 October 2022; Revised 10 January 2023; Accepted 30 January 2023; Published 24 March 2023

Academic Editor: Lin Chen

A finite difference algorithm that evaluates the health conditions of a bonded joint is presented and discussed. The mathematical formulation of the problem is developed, paying particular attention to the singularity around the corners of the joint and implementing an original discretisation method of the partial differential equations governing the propagation of the elastic waves. The equations are solved under the only hypothesis of a bidimensional field. The algorithm is sensible to defects in the bonded joint and can be used as an effective structural health monitoring tool, as proven by the experiments that show close agreement with the numerical simulations.

1. Introduction

Adhesive bonding is an effective alternative to riveting and welding when lightweight structures are designed. In the aerospace and automotive industries, the use of adhesion is more and more pronounced, especially since when metals have often been replaced by composites for their high strength-to-weight ratio. When the application of the adhesives is related to structural parts demanding in terms of strength and/or fatigue requirements, the concern of the structural monitoring of the bonding integrity can rise [1–4]. Structural health monitoring (SHM) has received growing interest with multiple applications oriented to the development of damage/defect detection systems able to allow the transition from scheduled maintenance to condition-based maintenance in several areas [5–8]. An effective SHM method is the result of a reliable mathematical description of the structural part under control and the subsequent implementation of this model into a monitoring technique [9–11]. A number of studies were conducted in the last three decades about the inspection of adhesive joints using different methods that can be categorised according to the physical principle they are based on ultrasounds [12–14], X-rays [15], and thermography [16]. In the present paper, we employ a particular ultrasonic technique.

Mathematically, the presence of damage (debonding) in the joint can be seen as a discontinuity in velocity values for the elastic waves traveling in it: finite difference methods (FDMs) have been extensively used to develop mathematical models describing elastic waves propagation in structures [17, 18]. Other mathematical works are focused on modelling singularities around the corners such as the ones in single lap joints or at the crack's tips [19, 20]. In [21], an integral equation describing the stress field at a rounded *V*-shaped notch or hyperbolic notch (with an equal opening angle) is numerically solved through the complex variables theory: the main outcome of this work is that the singularity

of a sharp notch can be effectively handled considering the asymptotic behaviour of a rounded notch.

In [22], the authors propose a novel technique for the solution of Laplace problems describing the two-dimensional stress field around obtuse, or reentrant, corners: the real parts of rational functions, for which the poles cluster around the obtuse corners, are used to approximate the boundary solution. In [23], the problem of the singularity at the obtuse corners of adhesive joints is addressed using an alleviation factor called stress concentration limiter. The intense stress gradients around the obtuse corners are alleviated through a finite element algorithm describing how the stress is actually attenuated in singularity points.

From an engineering point of view, the monitoring technique of adhesive joints by ultrasounds is based on different possible algorithms. The basic principle of the technique is that an ultrasonic wave is passed through the material and is then reflected and/or mode converted by a defect [24]. A transmitter excites ultrasound waves into the structure, and the obtained signal is picked up by a receiver. In the simplest arrangement, the transmitter and receiver are placed on opposite surfaces of the specimen [25–28]. More specifically, Lamb waves can be used to detect defects in bonded joints. Nicassio et al. exploit the linear interference [29] and nonlinear interaction [30, 31] of elastic waves to characterise the health conditions of metal joints. In [32], a scanning laser Doppler vibrometry is used to monitor the health conditions of adhesive joints stimulating Lamb waves propagation: a damage imaging is successfully achieved. In [33], ultrasonic-guided waves are used to monitor the interfacial mechanical properties between solid bodies in contact. The main results of this study indicate that the applied load affects the attenuation and induces mode conversion of the studied *S*0 vibration mode.

In this manuscript, the development of an FD 2D model of a single lap joint (SLJ) is presented and discussed. A structural health monitoring technique using Lamb waves propagation was numerically developed. Because, in common and practical cases, the joint fails at the edges of the overlap where the stress is higher, the aim of the proposed technique was the use of the Lamb wave propagations to verify the state of the adhesive region and estimate the size of possible disbonds into the overlap area. The present paper is divided into two main parts: in the first part, a novel mathematical model of a three layers bonded joint crossed by ultrasonic waves and its numerical implementation are presented and discussed; in the second part, experiments on an SLJ are carried out by using two PZT sensors attached on the upper and lower plate in pitch and catch configuration. The *S*0 mode is used to investigate the integrity of adhesive in the bonded zone. Frequencies below the cut-off value are used in order to avoid the presence of higher symmetric and antisymmetric modes. The received signals are transformed by short time fourier transform (STFT) in order to correlate frequency spectra to the structural health of the adhesive. Several wave packets with different driving frequencies are used to investigate the bonded area. Experiments reveal, in agreement with numerical simulations, that there is a specific exciting frequency (per each damage characteristic length) at which the signal is attenuated. The main novelty of this work is the development of a mathematical technique based on the use of the finite difference method to discretise the 2D problem of the single lap joint that is able to mitigate the singularity at the corners: a novel reduced-order FD model is obtained, and it appears simpler, cleaner and easier than FE model. In view of industrial applications, one point of strength of the proposed study is that numerical simulations can be carried out by a relatively simple and novel MATLAB code with a short computational load.

2. Material and Methods

2.1. Mathematical Model

2.1.1. State of Art Investigation and Background. The mathematical model stems from the Cauchy–Navier equation for elastodynamics with nonconstant Lamé coefficients. Indeed, the key feature lies in the fact that the space-dependent Lamé coefficients are locally constant, with discontinuity on the boundary with the debonded region. This implies that it is possible to find a finite difference discretisation of the Cauchy–Navier equations that is insensitive to the singularities between the go through a smooth transition with a steep gradient between the different layers, which is close to the physical situation.

The discretisation of the Cauchy–Navier system is performed by a second-order scheme that follows existing literature but introduces new elements as well. In particular, in [34],traveling wave solutions to the equations of surface waves in a piezoelectric-hydrogel layer on an elastic substrate are found in an analytic way. The setup has some point of contact with ours, being a layered structure with homogeneous layers of different materials. However, traveling wave solutions for our equations are much more difficult to obtain, as the system and the geometry of its domain are both much more complicated than in the case considered by the authors. Also in [35], specific waves (love ones) are used to solve the Cauchy–Navier problem. This approach is too simple in terms of geometrical domain and numerical algorithm, and hence not appropriate for our test case. In the paper [36], it is proved that, for constant Lamé moduli, the discretisation is second-order accurate and energy conservative, hence stable on a domain that is a parallelepiped or a box. It is noteworthy that Nilsson's work considers isotropic materials subject to a stress-free boundary condition, and this scenario allows an easier wave equation formulation. Another second-order finite difference approach with variable Lamé moduli and on a box can be found in [37], despite no experimental correlation and relative validation provided.

In our paper, we extend the same discretisation to Lamé moduli that are separately constant on each layer of the bonded joint. Moreover, our domain is the union of adjacent but displaced boxes. While, due to these two factors, it is not easy to extend the previously mentioned mathematical results, the scheme is a direct generalization of that in [36]. More precisely, the discretisation preserves the structure of the obvious conservation laws (in the absence of external

forces), and it is made by second-order approximations. This allows us to take into account the contribution of the derivatives of the Lamé coefficients across the discontinuity.

In our model, the treatment of corners is one of the most delicate points. Acute corners are dealt with by means of boundary conditions, external pseudonodes, and an original approach to discretized derivatives. On the other hand, we introduce a new technique to deal with obtuse corner singularities in the numerical method. The singularities exist only in the virtual reality of the mathematical model, as the physical setup does not have perfectly sharp corners; the attenuation factor allows us to get rid of the virtual singularities in an elegant way and yields a result that is a perfect match with the experiments. Note that the presence of "virtual" singularities makes a mathematical convergence analysis difficult, also in view of the results in [22].

It should be observed that some higher-order finite difference schemes for Cauchy–Navier equations have been proposed in the literature [38] (see also [39]). However, the usefulness of our approach is that the speed of convergence of our second-order scheme is so high that we did not feel the need for a more accurate (and more complicated) method presented in the technical literature.

A preliminary simpler version of the FD method was developed by the authors in [40]. The most significant differences between the present work and the previous one are the following:

(i) For the geometry, in the previous work a homogeneous area simulated the overlapped zone, while in the present one, a 3-boxes approach is followed with a complete model of the experimental sample

(ii) For what concerns the finite difference method, previously, the Cauchy–Navier equations were differentiated, and then all the derivatives were discretized, now a new discretisation operator is adopted, preserving the physical meaning of the terms

(iii) In the previous model, only acute corner pseudonodes were used, while in the current one, acute and obtuse corner pseudonodes are used

(iv) In the present paper, a singularity attenuation factor is introduced

More specifically, despite the good agreement between numerical and experimental results in [40], the homogenization approach concerning the overlap area is a weakness of the previous approach since the interaction between the layers in the joint area (aluminium—adhesive—aluminium), with the differences in wave speed through the layers, was completely lost. Moreover, in the present approach, the mechanical properties of the entire joint can easily modified without additional homogenization tools. In terms of geometry, the absence of obtuse angle in [40] leads to a weak solution; actually, the maximum stresses grow out of an obtuse areas and cause the disbonds studied in these two works. The presented FD model allows us to evaluate the stress evolution for the entire SLJ, thanks to the singularity attenuation factor introduced in the obtuse zones.

2.1.2. The System of PDEs and the Stress-Free Conditions. In this section, we will derive the mathematical model that we will use to predict the results of the experiments. We will use the theory of linear elasticity in two space dimensions. The partial differential equations of the theory will be set up in a form that will be the most suitable for the numerical solution. Our source is [41].

The dynamics of a continuum body on $\Omega \subseteq \mathbb{R}^2$ is modelised by equations of the local balance of linear and angular momentum as follows:

$$\rho \mathbf{u}_{tt} = \nabla \cdot S + \rho \mathbf{f}, \tag{1}$$

where $\mathbf{u} = (u, v)^T$ is the displacement vector field, whose components u and v are the unknown functions in our problem. Moreover, ρ is the density of the medium, S is the Piola–Kirchhoff stress tensor and $\mathbf{f} = (f^1, f^2)^T$ is the body strength measured per unit of volume. Let us define $\mathbf{H} = \nabla \mathbf{u}$. The infinitesimal strain tensor is defined as $\mathbf{E} = 1/2\,(\mathbf{H} + \mathbf{H}^T)$. Under the hypothesis of isotropic linear elasticity, the Piola–Kirchhoff tensor takes the following form:

$$\begin{aligned} \mathbf{S} &= \lambda(x, y)(\mathrm{tr}\mathbf{E})\mathbf{I} + 2\mu(x, y)\mathbf{E}, \\ &= \lambda(x, y)\begin{pmatrix} u_x + v_y & 0 \\ 0 & u_x + v_y \end{pmatrix} + 2\mu(x, y)\begin{pmatrix} u_x & \dfrac{u_y + v_x}{2} \\ \dfrac{u_y + v_x}{2} & v_y \end{pmatrix}, \end{aligned} \tag{2}$$

where λ and μ are the Lamé moduli. By substituting $\mathbf{S}$ into the main equation (1) and dividing by ρ the Cauchy–Navier system of partial differential equations (PDEs) governing the phenomenon is explicitly given.

$$u_{tt} = \frac{1}{\rho}\left[S_x^{11} + S_y^{21}\right] + f^1 = \frac{1}{\rho}\left[(\lambda u_x)_x + (\lambda v_y)_x + 2(\mu u_x)_x + (\mu u_y)_y + (\mu v_x)_y\right] + f^1, \tag{3}$$

$$v_{tt} = \frac{1}{\rho}\left[S_x^{12} + S_y^{22}\right] + f^2 = \frac{1}{\rho}\left[(\mu u_y)_x + (\mu v_x)_x + (\lambda u_x)_y + (\lambda v_y)_y + 2(\mu v_y)_y\right] + f^2. \tag{4}$$

The Lamé moduli depend on the physical properties of the medium. In our case, the medium has constant physical properties separately in each of the three different regions of the SLJ (two aluminum plates and adhesive layer), with a discontinuity between the metal and the glue. This means that our Lamé moduli will be piecewise constant functions, with jump discontinuities on the internal boundaries between metal and glue.

The previously mentioned feature of our model implies that it is better to keep the gradients in previously mentioned equations (3) and (4) in nonexpanded form for a discretisation that preserves the obvious conserved quantities, as we will see in the next section.

We will produce concentrated stress at one end of our experimental setup; this will create waves that propagate through the domain. This is modelled as a force $\mathbf{f}$ that is defined as follows:

$$t \mapsto \begin{cases} F(t), & \text{if } t \in [t_I, t_F], \\ 0, & \text{otherwise,} \end{cases} \tag{5}$$

with,

$$F(t) = A\left[1 - \cos\left(\frac{2\pi\nu}{N_i}(t - 2\Delta t)\right)\right]\sin\left(2\pi\nu(t - 2\Delta t)\right), \tag{6}$$

where A is a given amplitude, $t_I = 2\Delta t$, N_i is the number of impulses of the probe signal, ν is the frequency of the probe signal and $t_F = N_i/\nu + 2\Delta t$. This is the source of the mechanical impulse, and it is a smoothed tone burst obtained from a pure tone filtered through a Hanning window (for a bell-shaped signal spectrum centered at the desired frequency). The choice of N_i and the frequency determines the length of the wave packet. The produced signal and the relative FFT are plotted in Figure 1.

We require stress-free boundary conditions on all the upper and lower horizontal sides of the plates, whereas conditions of free ends are required on all vertical sides (see Figure 2(a)).

Let us define,

$$c_L^2 = \frac{\lambda + 2\mu}{\rho}, \qquad c_T^2 = \frac{\mu}{\rho}, \tag{7}$$

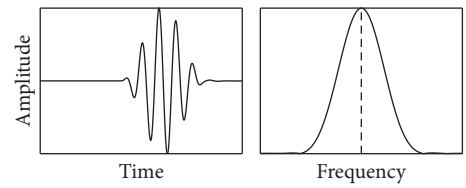

Figure 1: Toneburst signal.

the longitudinal and shear wave speeds, respectively. Let us stress that the functions c_L, c_T, and ρ are nonconstant functions of (x, y).

Then, stress-free conditions are modelled by the following conditions holding on horizontal boundaries:

$$\left(c_L^2 - 2c_T^2\right)u_x + c_L^2 v_y = 0, \tag{8a}$$

$$c_T^2\left(u_y + v_x\right) = 0, \tag{8b}$$

while the conditions of free-ends for vertical boundaries are as follows:

$$c_L^2 u_x + \left(c_L^2 - 2c_T^2\right)v_y = 0, \tag{9a}$$

$$c_T^2\left(u_y + v_x\right) = 0. \tag{9b}$$

2.1.3. Finite Difference Model. We will provide a numerical solution for systems (3) and (4) by a finite difference method.

There are several good reasons for the choice that we made, in particular:

(i) The domain Ω of our problem is regular enough to make an implementation of a finite difference method relatively simple. We thus avoid the use of sophisticated finite element proprietary software and allow a much easier and open reproducibility of our results;

(ii) We wrote a "pure" MATLAB code (i.e., with no use of additional packages such as PDEtools) that can also be run with minor changes on free MATLAB language emulators such as Octave, thus making an industrial use even more cheap;

(iii) The moderate use of computational resources that we make in our code allows us to run it on a desktop computer or on a laptop in a relatively short time;

(iv) The same computational features allow straightforward future extension to 3d structural health monitoring.

In order to represent the domain of the experiment, we have developed a 3-boxes approach (see Figure 2(a)). The first and the third grey boxes have the same geometric and mechanical properties and describe the two aluminum panels. The second (yellow) box represents the glue layer.

This approach leads to several advantages in computations. First of all, we can use different couples of variables in

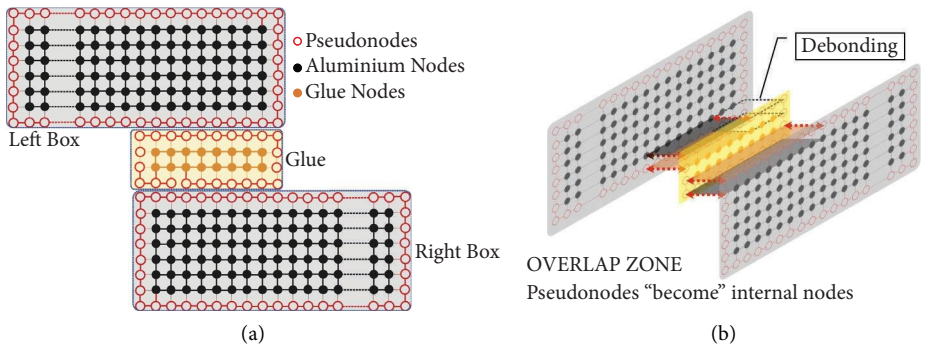

FIGURE 2: Graphic representation of used discretisation approach. (a) Three boxes. (b) Three boxes connections.

the boxes, for example u^1 and v^1 in the first box and analogously in the other boxes. This makes the code clearer, and it is easier to identify the waves along the panels. Secondly, it is easier to deal with boundary conditions, as each box has a very simple rectangular shape. It is then easy to let the values of variables on coinciding boundary points be the same.

Indeed, the key point of this approach is the connection between the boxes. As described in Figure 2(b), the connection is implemented by overlapping a line of points for each pair of boxes (left plate and glue; glue and right plate). In this area, the value of the variables is set to coincide.

This scheme is also very useful when the debonding area is introduced in the model (see Figure 2(b)). In this case, it is sufficient to keep in connection only a part of the overlapped points, whereas the nonconnected ones are treated as external boundary points.

Following the previously discussed ideas, we introduce three rectangular uniform grids on the three boxes, with spacing Δx and Δy along the two axes. We use three different couple of variables (one for each box) such that.

(i) (u^1, v^1) are functions of (x, y, t) on $I_{1x} \times I_{1y} \times I_t$, where $I_{1x} = [0, l_{Px}]$ and $I_{1y} = [0, l_{Py}]$. The first box is $I_{1x} \times I_{1y}$

(ii) (u^2, v^2) are functions of (x, y, t) on $I_{2x} \times I_{2y} \times I_t$, where $I_{2x} = [0, l_{Gx}]$ and $I_{2y} = [0, l_{Gy}]$. The second box is $I_{2x} \times I_{2y}$

(iii) (u^3, v^3) are functions of (x, y, t) on $I_{3x} \times I_{3y} \times I_t$, where $I_{3x} = [0, l_{Px}]$ and $I_{3y} = [0, l_{Py}]$. The third box is the same as the first box.

The time interval is $I_t = [0, l_t]$ for all boxes. We choose a time step Δt in such a way that the CFL stability condition is fulfilled as follows:

$$\Delta t \leq \frac{\Delta x}{\sqrt{c_L^2 + c_T^2}}. \tag{10}$$

The positive numbers l_{Px}, l_{Py}, l_{Gx}, l_{Gy}, l_{Px}, and l_{Py} are taken in such a way that the numbers.

$$\begin{aligned} M_1 &= M_3 = \frac{l_{Px}}{\Delta x} + 2, \\ N_1 &= N_3 = \frac{l_{Py}}{\Delta y} + 2, \\ M_2 &= \frac{l_{Gx}}{\Delta x} + 2, \\ N_2 &= \frac{l_{Gy}}{\Delta y} + 2, \end{aligned} \tag{11}$$

are integers. Then, every point on the box $\alpha\,(\alpha = 1, 2, 3)$ is identified by (x_i^α, y_j^α) with $1 \leq i \leq M_\alpha$ and $1 \leq j \leq N_\alpha$, where

$$\begin{aligned} x_1^1 &= 0, \\ x_{M_1}^1 &= l_{Px} + 2\Delta x, \\ x_1^2 &= 0, \\ x_{M_2}^2 &= l_{Gx} + 2\Delta x, \\ x_1^3 &= 0, \\ x_{M_3}^3 &= l_{Px} + 2\Delta x, \end{aligned} \tag{12}$$

and

$$\begin{aligned} y_1^1 &= 0, \\ y_{N_1}^1 &= l_{Py} + 2\Delta y, \\ y_1^2 &= 0, \\ y_{N_2}^2 &= l_{Gy} + 2\Delta y, \\ y_1^3 &= 0, \\ y_{N_3}^3 &= l_{Py} + 2\Delta y. \end{aligned} \tag{13}$$

In order to describe the numerical approximations of equations (3) and (4), we denote by $u_{i,j} = u_{i,j}(t) = u(x_i, y_j, t)$ the value of the displacement at the point (x_i, y_j) of the grid in one of the three boxes (i and j are suitable

integers) and at a generic time t; we will use a similar notation for all other functions involved.

In order to discretise the derivatives in equations (3) and (4), the most straightforward idea would be to use the chain rule on the terms of the form $\partial/\partial x\,(\lambda(x,y)u_x)$ and then discretise the resulting terms using the standard finite difference formulas for derivatives. Nevertheless, as pointed out in [42], this is not a good idea, especially when there are large jumps in the coefficient (and that is precisely our case). The discretisation that we will use is motivated by the fact that it preserves the conservative structure of the equations. Another feature of our discretisation is that the term λu_x represents a tension, and a direct discretisation of its derivative preserves its physical meaning. For these reasons, at every internal point (x_i, y_j) in the three boxes we introduce the discretisation operator D_x as follows:

$$\left(\lambda(x,y)u_{xx}\left(x_i,y_j,(t)\simeq D_x\left(\lambda(x,y)u_x\right)\right|_{i,j}=\frac{1}{\Delta x}\left(\lambda\left(i+\frac{1}{2},j\right)u_x\left(x_{i+1/2},y_j,t\right)-\lambda\left(i-\frac{1}{2},j\right)u_x\left(x_{i-1/2},y_j,t\right)\right), \tag{14}$$

where the terms u_x are further discretized as follows:

$$\begin{aligned} u_x\left(x_{i+1/2},y_j,t\right)&\simeq D_x(u)\big|_{i+1/2,j}=\frac{u_{i+1,j}-u_{i,j}}{\Delta x},\\ u_x\left(x_{i-1/2},y_j,t\right)&\simeq D_x(u)\big|_{i-1/2,j}=\frac{u_{i,j}-u_{i-1,j}}{\Delta x}, \end{aligned} \tag{15}$$

and analogously for all other second order nonmixed derivative terms. The coefficient $\lambda(i+1/2, j)$ can be computed as the arithmetic mean.

$$\lambda\left(i+\frac{1}{2},j\right)=\frac{1}{2}\left[\lambda(i+1,j)+\lambda(i,j)\right], \tag{16}$$

In a similar way.

$$\lambda\left(i-\frac{1}{2},j\right)=\frac{1}{2}\left[\lambda(i-1,j)+\lambda(i,j)\right], \tag{17}$$

and analogously for μ.

The terms with mixed derivatives are discretized as follows:

$$\begin{aligned} &\left(\lambda v_y\right)_x\left(x_i,y_j,t\right)\simeq D_x\left(\lambda v_y\right)\big|_{i,j}\\ &=\frac{1}{\Delta x}\left[\lambda\left(i+\frac{1}{2},j\right)v_y\left(i+\frac{1}{2},j\right)-\lambda\left(i-\frac{1}{2},j\right)v_y\left(i-\frac{1}{2},j\right)\right], \end{aligned} \tag{18}$$

where the "internal" derivative is approximated by an incremental ratio of two arithmetic means:

$$v_y\left(i-\frac{1}{2},j\right)\simeq\overline{D}_y(v)\big|_{i-1/2,j}=\frac{1}{4\Delta y}\left[v_{i,j+1}+v_{i-1,j+1}-v_{i,j-1}-v_{i-1,j-1}\right], \tag{19a}$$

$$v_y\left(i+\frac{1}{2},j\right)\simeq\overline{D}_y(v)\big|_{i+1/2,j}=\frac{1}{4\Delta y}\left[v_{i+1,j+1}+v_{i,j+1}-v_{i+1,j-1}-v_{i,j-1}\right]. \tag{19b}$$

Other mixed derivative terms are treated in the same way. The numerical approximation of the system (3) and (4) is thus completed on all internal points of the domain.

A significant problem is represented by the nodes on the boundary of the domain. We will calculate the numerical approximation of the system by means of external pseudonodes. The pseudonodes are located in the three boxes according to the pattern of empty red dots in Figure 2(a). The values of the displacements at the pseudonodes at each time step t_k are calculated from the boundary conditions as follows.

Let us consider the case of bottom horizontal line segments on the boundary: here $v_{i,j-1}$ and $u_{i,j-1}$ are unknown. The discretisation of the horizontal boundary conditions (8(a)and 8(b)) leads to the following system:

$$C\frac{u_{i+1,j}-u_{i-1,j}}{2\Delta x}+\frac{v_{i,j}-v_{i,j-1}}{\Delta y}=0, \tag{20a}$$

$$\frac{u_{i,j}-u_{i,j-1}}{\Delta y}+\frac{v_{i+1,j}-v_{i-1,j}}{2\Delta x}=0, \tag{20b}$$

where

$$C=\frac{c_L^2-2c_T^2}{c_L^2}. \tag{21}$$

By using (20(b) and 20(a)), it is possible to compute the unknown values of $u_{i,j-1}$ and $v_{i,j-1}$.

The remaining values of u and v to be computed are at the pseudonodes on the corners of the domain. We will treat separately the acute and the obtuse (or reentrant) corners.

First of all, let us notice that we can use all boundary conditions (8) and (9) at the corners. This yields the conditions,

$$\begin{aligned} u_x&=0,\\ v_y&=0,\\ u_y&=-v_x, \end{aligned} \tag{22}$$

on all corners.

Let us start with acute corners, and consider the ghost node on the upper leftmost corner of our domain. The values

of the displacements that we need to find are $u_{i-1,j+1}$ and $v_{i-1,j+1}$. The directional derivative of u along the line $x = -y$ is as follows:

$$\begin{aligned}\nabla u \cdot \left(-\frac{1}{\sqrt{2}}, \frac{1}{\sqrt{2}}\right) \\ = -\frac{1}{\sqrt{2}}u_x + \frac{1}{\sqrt{2}}u_y \\ = \frac{1}{\sqrt{2}}u_y,\end{aligned} \tag{23}$$

using the boundary conditions (22). The left-hand side of the previous equation has the second-order numerical approximation.

$$\frac{u_{i-1,j+1} - u_{i+1,j-1}}{2\sqrt{\Delta x^2 + \Delta y^2}}. \tag{24}$$

Using a second-order numerical approximation of u_y and equating the two approximations, we get the equation.

$$\frac{u_{i-1,j+1} - u_{i+1,j-1}}{2\sqrt{\Delta x^2 + \Delta y^2}} = \frac{1}{\sqrt{2}} \frac{u_{i,j+1} - u_{i,j-1}}{2\Delta y}, \tag{25}$$

that yields the unknown value of the "diagonal" ghost node $u_{i-1,j+1}$ in terms of "horizontal" and "vertical" ghost nodes $u_{i-1,j}$ and $u_{i,j+1}$ and the internal node $u_{i+1,j-1}$.

The values of the displacement u (as well as that of v) on other acute corners can be computed in the same way. The abovementioned treatment of the corners, although simple, seems to be another novelty element of our numerical model.

A different treatment turns out to be necessary when we deal with the internal obtuse corners of our domain. We stress that the way in which we simulate a debonding yields four obtuse corners (see Figure 2(a)). As shown in Figure 3(a), the four obtuse corners are represented by four internal nodes of the boxes. It follows that the value of variables u and v can be computed by using the eight adjacent nodes. Such corners are known in literature [21, 22] for generating singularities of the stress; indeed, numerical simulations show a divergence of our numerical model exactly on the obtuse corners if no special care is taken.

There could be several ways to deal with the problem. The simplest idea is to increase the number of grid points, at least around the singular corners. Unfortunately, this idea does not work, as the refinement of the grid has a negative influence on the strength of the singularities. A possible idea in the literature is to approximate the solution in the corners using functions with singularities, either in an ansatz or asymptotic estimate of an exact solution or as finite elements [22, 43].

Our way follows from the consideration that in our physical situation such corners are not sharp in reality, and we can think that they are round at a microscopic scale. Indeed, no divergence can be observed in experiments; on the theoretical side, this can be realised as in [21, 44, 45]. Note that the homogeneous part of the systems (3) and (4) is invariant with respect to a simultaneous change in scale in x and y, and that the force can be changed accordingly. This shows that the behaviour of the solution at the singular point is scale-independent (see [44]).

In [44], an accurate approximate solution u of the Laplace equation on a domain with a reentrant corner O is built from a solution close to the corner, which is self-similar and singular at the corner, and an exact solution far from the corner, which is not influenced by the values at the singularity. Due to the greater simplicity of the equation in [44] (but see also [21]) an asymptotic estimate of the exact solution is provided.

In our case, an asymptotic analysis of the exact solution of the systems (3) and (4) is unpractical, due to the greater complexity of the system. However, we can assume that the singularity is in the derivatives of the solution at the obtuse corners, as the value of the solution does not have big increments in experimental data and due to the fact that reentrant corners are points at the boundary between materials, where the Lamé moduli have a jump discontinuity.

This leads us (see Figure 3(b)) to the direct use of a singularity attenuation factor: at each time step of the numerical method, we evaluate values of u and v at the nodes closer to the reentrant corners (in the Ω_ε subdomain, dotted circle in Figure 3(b)) by a multiple $\mathscr{K}u$ and $\mathscr{K}v$, where $0 < \mathscr{K} < 1$ (purple lines in Figure 3(b)).

The presented approach is a "support algorithm" that simulates the attenuation of stresses in regions of high-stress gradients, particularly present around singular points. It smoothens these high gradients by $\mathscr{K}$: it redistributes the stresses (by acting on u and v), producing a new stress state that converges. Basically, this parameter determines the region over which numerical stresses must be reduced. The working of the singularity attenuation factor can be explained as follows: to obtain the stress distribution in the presented domain (see Figure 3(b)), the first step is to build a regular FD model; then, per each integration time step, weighted displacements (i.e., stress values) are determined in Ω_ε. The attenuation factor $\mathscr{K}$, the value of which is chosen according to observations that will be subsequently discussed, is extremely sensitive to grid density. To justify the use of the $\mathscr{K}$, two conditions have to be satisfied by the FD grid. First of all, the mesh must be sufficiently refined to accurately represent the actual geometry of the SLJ and its mechanical properties. Convergence of stress values in regions that are not affected by stress singularities must be established. Then $\mathscr{K}$ should be used to ensure the additional convergence of stresses only around singular locations. Secondly, the mesh should be sufficiently refined to allow $\mathscr{K}$ to affect the stress distribution in Ω_ε. If the distance between the grid points is too large, the effect of the singularity attenuation factor is too small.

The proposed approach aims to find the bigger value $\mathscr{K}$ that reduces Ω_ε in the unique obtuse corner node, for fixed Δx and Δy (see Results Section). With regard to Figure 3(b):

(a) $0.975 < \mathscr{K} < 1 \Rightarrow$ a completely convergent stress/strain distribution can never be obtained since

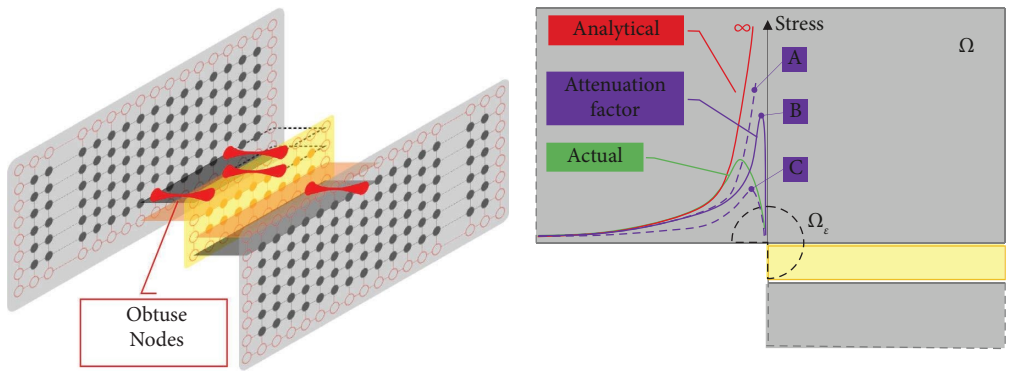

(a) (b)

FIGURE 3: Obtuse corners approach. (a) Treatment of obtuse corners. (b) Graphic representation of Ω and the singularity attenuation factor effect.

displacement field singularities locally cause stresses and strains to diverge with these values of $\mathcal{K}$

(b) $\mathcal{K} = 0.975 \Rightarrow$ it is enough to obtain the convergence of the numerical method, with Ω_ε that subtends just the only obtuse corner node

(c) $\mathcal{K} < 0.975 \Rightarrow$ a completely convergent stress/strain distribution can always be obtained, but too conservative values of $\mathcal{K}$ provide a nonrealistic model behaviour (too conservative stress evaluation with respect to the actual one, green line in Figure 3(b))

Summarizing, the main factors that impact the accuracy of the proposed approach are (i) mesh dimensions Δx and Δy, (ii) singularity attenuation factor $\mathcal{K}$, and (iii) simulation time step Δt.

A similar approach was implemented in [23] by using a stress concentration limiter that simulates the local attenuation of stresses around singular nodes, as it occurs in empirical observations. This approach makes use of spatially averages through exponential weight functions at the nearest nodes to the singular one. In a different way, our factor acts exactly on the value of the displacements at the singular node, previously computed using the adjacent nodes.

The numerical model is completed by the discretisation of the time derivatives u_{tt}, v_{tt} by means of the usual centred second order approximation. Let us denote the values of displacements in an arbitrary box (note that we are not using the indices that refer to a specific box) at the time t^k by $u^k_{i,j} = u(x_i, y_j, t^k)$, $v^k_{i,j} = v(x_i, y_j, t^k)$. Then, the values of the displacements at the time t^{k+1} are given by explicit formulas.

$$u^{k+1}_{i,j} = 2u^k_{i,j} - u^{k-1}_{i,j} + \frac{(\Delta t)^2}{\rho_{i,j}}\left[D_x(\lambda D_x u)\big|^k_{i,j} + D_x\left(\lambda \overline{D}_y v\right)\big|^k_{i,j} + 2D_x(\mu D_x u)\big|^k_{i,j} + D_y\left(\mu D_y u\right)\big|^k_{i,j} + D_y(\mu \overline{D}_x v)\big|^k_{i,j}\right] + f^1\big|^k_{i,j}, \tag{26a}$$

$$v^{k+1}_{i,j} = 2v^k_{i,j} - v^{k-1}_{i,j} + \frac{(\Delta t)^2}{\rho_{i,j}}\left[D_x\left(\mu \overline{D}_y u\right)\big|^k_{i,j} + D_x(\mu D_x v)\big|^k_{i,j} + D_y(\lambda \overline{D}_x u)\big|^k_{i,j} + D_y\left(\lambda D_y v\right)\big|^k_{i,j} + 2D_y\left(\mu D_y v\right)\big|^k_{i,j}\right] + f^2\big|^k_{i,j}, \tag{26b}$$

in terms of the values of displacements at previous times t_k and t_{k-1}.

2.2. The Experimental Setup. Two aluminium plates (630 mm × 126 mm × 1.2 mm) were used to manufacture several SLJ samples (see Figure 4). Artificial defects (disbonds) were introduced in the overlap zone of 30 mm (nominal adhesive thickness of 0.3 mm) with increasing debonding values Deb of 3–5–7.5–10–12.5–15 mm. Teflon sheets were carefully used during the SLJ manufacturing process to reproduce actual damages. The materials' properties are as follows:

(i) 2024 Aluminium alloy

Modulus of elasticity = 72 GPa
Density = 2770 kg/m^3
Poisson's ratio = 0.33

(ii) Adhesive

Modulus of elasticity = 3.69 GPa
Density = 1300 kg/m^3
Poisson's ratio = 0.3

Vibration-absorbing sponges under the sample were used to achieve stress-free conditions during the test campaigns.

In Figure 4, the experimental set-up is shown.

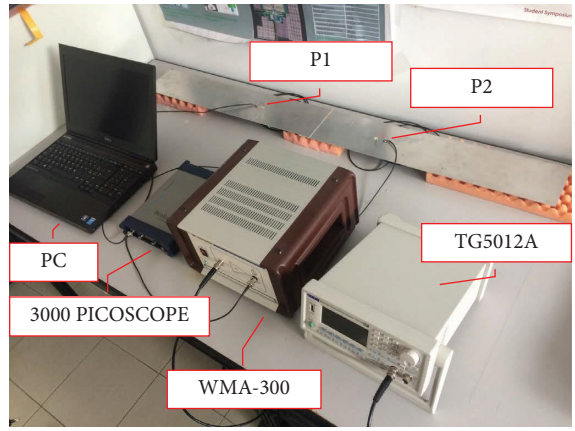

Figure 4: Experimental setup.

(1) The exciting signal to the sample is provided by the generator TG5012A of Aim and Thurlby Thandar Instrument

(2) The signal is powered (×50 the input voltage) by WMA-300 of the Falco System

(3) The piezo-sensor P1 (low harmonic distortion and phase noise, high-frequency resolution) is excited by the incoming signal

(4) The signal excites the overlap zone and the disbond region and comes into the receiver sensor P2

(5) The oscilloscope 3000 PicoScope captures and displays the waveforms by monitoring the signal and waiting for the voltage to rise above a set threshold (variable for each disbond length) via single trigger mode control

(6) All signals are low-pass filtered and processed by using software PicoScope 6 and MATLAB codes on PC in order to detect the differences for the various wave packets and to evaluate relative disbond lengths

3. Results and Discussions

Figures and Table present the main results of this work. The uniform space grid of the finite difference method was constructed with the following features.

(i) Δx equal to 0.5 mm is the greatest common divisor of Deb values (expressed as 1/10 mm) in order to have an integer number of nodes simulating the disbond

(ii) Δy is equal to 0.3 mm in order to correctly simulate the glue layer with at least one node and to obtain an integer number of plate thickness nodes

Smaller values of Δx and Δy imply a sensible increase in execution time and are not considered. Nevertheless, the gap between nodes is smaller than 1/40 of the bigger wavelength propagating in the SLJ excited at several frequencies. The uniform time grid of the FD problem Δt was constructed with a time interval equal to 1/4 of the CFL stability time value.

In Figure 5, spectrograms of the transient FD signals are reported at the top of each subfigure. The wave packet was generated with several frequency contents (see Table 1) and arrives at the box simulating the aluminium plate. The observation time window is reported on the y-axis of each spectrogram and represents the time evolution of the STFT applied to the transient signals. In each subfigure, the spectrogram is associated with a subplot representing the PSD (probability spectral density) of the signals, obtained by selecting a particular STFT at an instant of time.

The destructive interference, clearly represented in the FD spectrograms and PSD plots, is characterised by a strong amplitude attenuation at the exciting frequency ν_{att} related to the specific value of disbond. This amplitude attenuation can be associated in the spectrograms with "valleys" (in colour map blue represents low amplitude, yellow represents high amplitude): cutting the spectrograms at these "valleys" time coordinates, PSD plots are obtained representing the frequency content of the signal acquired at a specific instant of time: all these plots are characterised by a two "bell-shape" frequency spectrum that mean frequency values with very low amplitude. From these Figures, it is possible to evaluate the ν_{att} reported in Table 1 in column FDM.

In Table 1, the experimental, analytical, and numerical results are reported for comparison. The increasing debonding lengths are listed in the first column. Disbond lengths smaller than 3 mm (<10% of the overlap area) were not taken into account for manufacturing reasons. The experimental tests were performed five times per each value of Deb, to average the measurements and verify their repetitiveness. The third, fourth, fifth, and sixth columns report the excitation frequency value $\nu_{\text{ex}} = \nu_{\text{att}}$ for which destructive interference occurs. The superscript * indicates technical literature data reported in [29]. It can be seen in the Table that the percent error for all FDM ν_{att} is never more than 8% on the experimental results (last column), in the worst case being on average 4.4% in the comparison between experimental and FDM results. Furthermore, the FDM percent errors are comparable to FEM ones: the main feature of the presented FDM model is the small computational time consuming, few minutes vs. at least one hour for FEM simulations reported in [29].

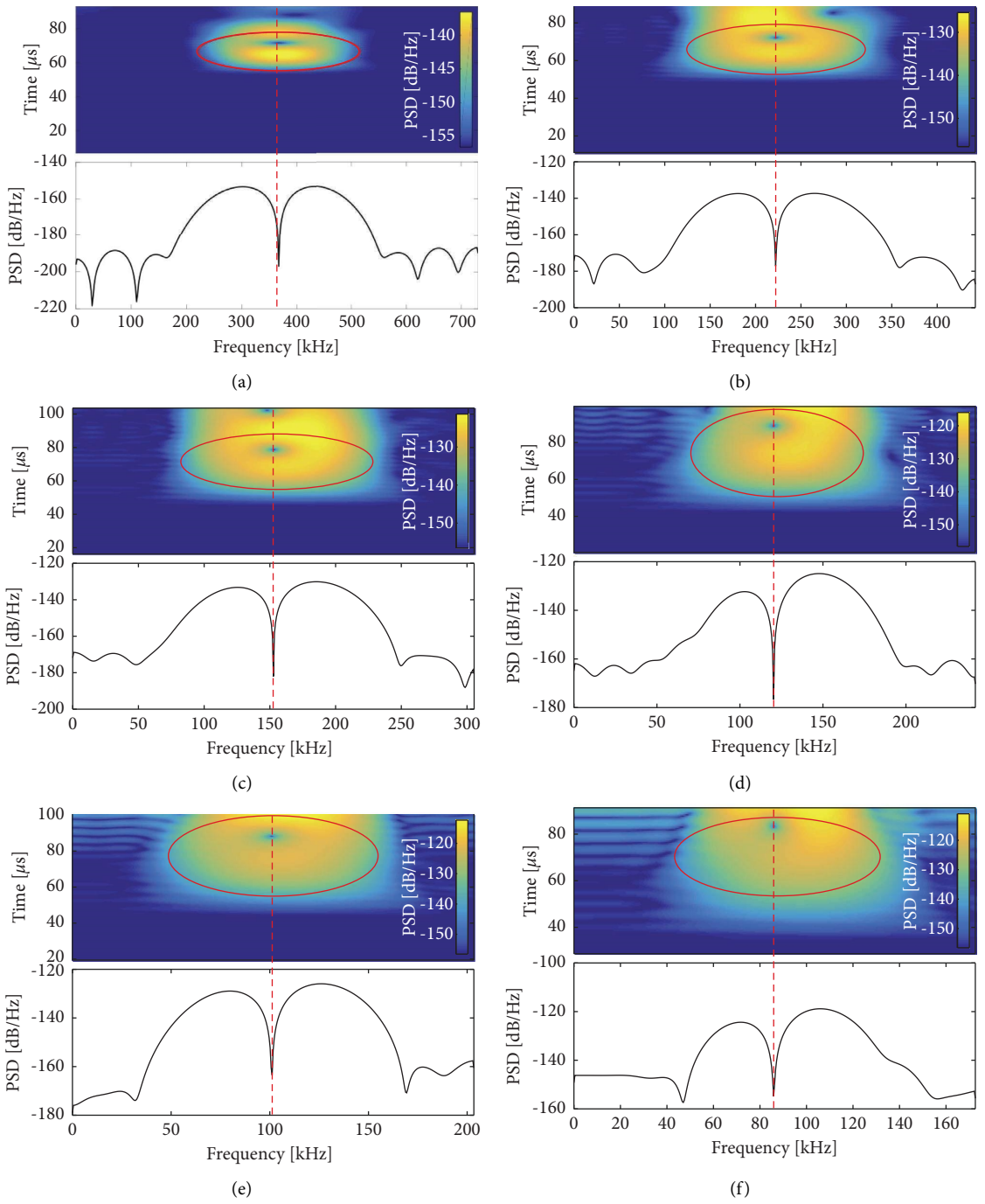

FIGURE 5: STFT and PSD plots for all Deb values. (a) Deb = 3 mm. (b) Deb = 5 mm. (c) Deb = 7.5 mm. (d) Deb = 10 mm. (e) Deb = 12.5 mm. (f) Deb = 15 mm.

TABLE 1: Debonding attenuation results.

Deb (mm)	N_i*	EXP.	AN.*	FEM*	FDM	EXP. Vs. FEM	EXP. Vs. FDM
			ν_{att} (kHz)			(%)	
3	8	344	352	320	**365**	−6.9	6.1
5	5	230	229	240	**215**	4.3	−6.5
7.5		155	153	165	**153**	6.4	−1.3
10		116	114	115	**121**	−0.9	4.3
12.5		95	92	92	**102**	−3.1	7.4
15	3	87	79	80	**86**	−8.0	−1.1

FDM data are written in bold to highlight the results of the presented manuscript with respect to experimental and literature data.

4. Conclusions

This article presents a novel 2D finite difference method model with an attenuation factor for structural health monitoring of single lap Joints.

The mathematical model is the Cauchy–Navier equation of linear elasticity with variable Lamé moduli. The corresponding system of two partial differential equations in two unknown functions of time and two space coordinates was solved using a novel finite difference method (grid of nodes and pseudonodes) for two thin plates connected by a glue layer and excited by Lamb waves. The presence of an overlap zone with damage (debonding) was simulated by means of a regular domain and a particular interaction between pseudonodes at the boundary. The numerical joint spectral response was carefully investigated to relate the damage to the signal content.

Fairly good experimental/numerical correlations were found in terms of specific frequencies for each value of disbond and relative signal attenuation representative of the damage. It is worth to remark the important role of the approach based on the use of a singularity attenuation factor in the processing of the pseudonodes on the obtuse (or reentrant) corners of the domain. This original method allows to dampen the displacements at the points in which the numerical method has a singularity that is not consistent with the physical facts.

In our opinion, there are strong reasons that make the method interesting.

(i) The numerical domain of the SLJ problem has a relatively simple geometry. Our custom code can be implemented in any programming language with minor changes. In particular, our code runs in Octave, which is a free software emulator of the Matlab language, with almost no change. Hence, we avoid relying on expensive proprietary codes.

(ii) The simplicity and low computational cost of the proposed method make it particularly interesting for future works (extension to 3D SHM model with punctual damage): the proposed approach solves 2D geometry (invariant behavior on the 3rd dimension). In this way, the method solves a geometry with endless damage, far from the actual scenario. Another point of interest is the further industrial application (i.e., online SHM on working structures).

(iii) We plan to publish the code that we used to calculate the solutions of the mathematical model in a separate paper in order to make our results completely accessible to the scientific community.

Data Availability

The datasets generated during and/or analysed during the current study are not publicly available but are available from the corresponding author upon reasonable request.

Conflicts of Interest

The authors declare that they have no conflicts of interest.

Acknowledgments

The authors are thankful to I. Sgura for useful discussions. The authors did not use any funds to perform the study discussed in the manuscript.

References

[1] V. Giurgiutiu, "Structural health monitoring (SHM) of aerospace composites," in *Polymer Composites in the Aerospace Industry*Elsevier, Amsterdam, Netherlands, 2019.

[2] D. G. Bekas, M. M. Mendias, Z. S. Khodaei, E. Karachalios, F. J. C. Alonso, and M. H. Aliabadi, "SHM of composite mono-stringer elements based on guided waves," in *Key Engineering Materials*Trans Tech Publications Ltd, Wollerau, Switzerland, 2022.

[3] D. Ginzburg, F. Ciampa, G. Scarselli, and M. Meo, "SHM of single lap adhesive joints using subharmonic frequencies," *Smart Materials and Structures*, vol. 26, no. 10, Article ID 105018, 2017.

[4] B. S. M. Ebna Hai and M. Bause, "Numerical study and comparison of alternative time discretization schemes for an ultrasonic guided wave propagation problem coupled with fluid–structure interaction," *Computers & Mathematics with Applications*, vol. 78, no. 9, pp. 2867–2885, 2019.

[5] T. Dong, R. Haftka, and N. Kim, "Advantages of condition-based maintenance over scheduled maintenance using structural health monitoring system," in *Reliability and Maintenance - an Overview of Cases*IntechOpen, London, UK, 2020.

[6] I. Benedetti, M. H. Aliabadi, and A. Milazzo, "A fast BEM for the analysis of damaged structures with bonded piezoelectric sensors," *Computer Methods in Applied Mechanics and Engineering*, vol. 199, no. 9-12, pp. 490–501, 2010.

[7] S. Yoon, B. F. Spencer, S. Lee, H. J. Jung, and I. H. Kim, "A novel approach to assess the seismic performance of deteriorated bridge structures by employing UAV-based damage detection," *Structural Control and Health Monitoring*, vol. 29, no. 7, Article ID e2964, 2022.

[8] Y. Xia, X. Lei, P. Wang, and L. Sun, "A data-driven approach for regional bridge condition assessment using inspection reports," *Structural Control and Health Monitoring*, vol. 29, no. 4, Article ID e2915, 2022.

[9] C. Bigoni, Z. Zhang, and J. S. Hesthaven, "Systematic sensor placement for structural anomaly detection in the absence of damaged states," *Computer Methods in Applied Mechanics and Engineering*, vol. 371, Article ID 113315, 2020.

[10] C. Bigoni and J. S. Hesthaven, "Simulation-based anomaly detection and damage localization: an application to structural health monitoring," *Computer Methods in Applied Mechanics and Engineering*, vol. 363, Article ID 112896, 2020.

[11] S. Kapuria and M. Jain, "AC 1-continuous time domain spectral finite element for wave propagation analysis of Euler–Bernoulli beams," *International Journal for Numerical Methods in Engineering*, vol. 122, no. 11, pp. 2631–2652, 2021.

[12] S. Saha Ray, "New exact solutions of nonlinear fractional acoustic wave equations in ultrasound," *Computers & Mathematics with Applications*, vol. 71, no. 3, pp. 859–868, 2016.

[13] X. Xue, X. Chen, X. Zhang, and B. Qiao, "Hermitian plane wavelet finite element method: wave propagation and load identification," *Computers & Mathematics with Applications*, vol. 72, no. 12, pp. 2920–2942, 2016.

[14] A. Imperiale, N. Leymarie, and E. Demaldent, "Numerical modeling of wave propagation in anisotropic viscoelastic laminated materials in transient regime: application to modeling ultrasonic testing of composite structures," *International Journal for Numerical Methods in Engineering*, vol. 121, no. 15, pp. 3300–3338, 2020.

[15] S. Zheng, J. Vanderstelt, J. R. McDermid, and J. R. Kish, "Non-destructive investigation of aluminum alloy hemmed joints using neutron radiography and X-ray computed tomography," *NDT & E International*, vol. 91, pp. 32–35, 2017.

[16] X. Li, J. Sun, N. Tao et al., "An effective method to inspect adhesive quality of wind turbine blades using transmission thermography," *Journal of Nondestructive Evaluation*, vol. 37, no. 2, pp. 19–11, 2018.

[17] M. Schneider, "On non-stationary polarization methods in FFT-based computational micromechanics," *International Journal for Numerical Methods in Engineering*, vol. 122, no. 22, pp. 6800–6821, 2021.

[18] M. I. Belishev and Y. V. Kurylev, "Boundary control, wave field continuation and inverse problems for the wave equation," *Computers & Mathematics with Applications*, vol. 22, no. 4-5, pp. 27–52, 1991.

[19] C. Huang, "Stress singularities at angular corners in first-order shear deformation plate theory," *International Journal of Mechanical Sciences*, vol. 45, no. 1, pp. 1–20, 2003.

[20] X. F. Li, G. J. Tang, and B. Q. Tang, "Stress field around a strike-slip fault in orthotropic elastic layers via a hypersingular integral equation," *Computers & Mathematics with Applications*, vol. 66, no. 11, pp. 2317–2326, 2013.

[21] A. Kazberuk, M. P. Savruk, and A. B. Chornenkyi, "Stress distribution at sharp and rounded V-notches in quasi-orthotropic plane," *International Journal of Solids and Structures*, vol. 85-86, pp. 134–143, 2016.

[22] A. Gopal and L. N. Trefethen, "Solving laplace problems with corner singularities via rational functions," *SIAM Journal on Numerical Analysis*, vol. 57, no. 5, pp. 2074–2094, 2019.

[23] J. Stolk, N. Verdonschot, and R. Huiskes, "Management of stress fields around singular points in a finite element analysis," in *A Computerized Pre-clinical Test for Cemented Hip Prostheses Based on Finite Element Techniques*Gordon and Breach Science Publishers, Philadelphia, PA, USA, 2022.

[24] V. Vlasie, S. de Barros, M. Rousseau, L. Champaney, H. Duflo, and B. Morvan, "Mechanical and acoustical study of a structural bond: comparison theory/numerical simulations/experiment," *European Journal of Mechanics - A: Solids*, vol. 25, no. 3, pp. 464–482, 2006.

[25] G. M. F. Ramalho, A. M. Lopes, and L. F. M. Silva, "Structural health monitoring of adhesive joints using Lamb waves: a review," *Structural Control and Health Monitoring*, vol. 29, no. 1, Article ID e2849, 2022.

[26] W. Wang, H. Zhang, J. P. Lynch, C. E. Cesnik, and H. Li, "Experimental and numerical validation of guided wave phased arrays integrated within standard data acquisition systems for structural health monitoring," *Structural Control and Health Monitoring*, vol. 25, no. 6, Article ID e2171, 2018.

[27] P. K. Motamed, A. Abedian, and M. Nasiri, "Optimal sensors layout design based on reference-free damage localization with lamb wave propagation," *Structural Control and Health Monitoring*, vol. 27, no. 4, Article ID e2490, 2020.

[28] X. Ding, X. Wang, Y. Li, L. Wang, and L. Zeng, "Two-step damage identification method for composite laminates using distributed piezoelectric and strain sensors," *Structural Control and Health Monitoring*, vol. 29, no. 4, Article ID e2913, 2022.

[29] F. Nicassio, S. Carrino, and G. Scarselli, "Elastic waves interference for the analysis of disbonds in single lap joints," *Mechanical Systems and Signal Processing*, vol. 128, pp. 340–351, 2019.

[30] F. Nicassio, S. Carrino, and G. Scarselli, "Non-linear lamb waves for locating defects in single-lap joints," *Frontiers in Built Environment*, vol. 6, p. 45, 2020.

[31] S. Carrino, F. Nicassio, and G. Scarselli, "Subharmonics and beating: a new approach to Local Defect Resonance for bonded single lap joints," *Journal of Sound and Vibration*, vol. 456, pp. 289–305, 2019.

[32] E. Wojtczak and M. Rucka, "Wave frequency effects on damage imaging in adhesive joints using lamb waves and RMS," *Materials*, vol. 12, no. 11, p. 1842, 2019.

[33] A. Balvantín, A. Baltazar, and J. I. Aranda-Sanchez, "A study of guided wave propagation on a plate between two solid bodies with imperfect boundary conditions," *International Journal of Mechanical Sciences*, vol. 63, no. 1, pp. 66–73, 2012.

[34] S. Chaudhary and S. S. Mulay, "A mathematical modelling of multiphysics-based propagation characteristics of surface wave in piezoelectric - hydrogel layer on an elastic substrate," *Applied Mathematical Modelling*, vol. 103, pp. 493–515, 2022.

[35] F. Billon and A. El Baroudi, "Mathematical modelling of Love waves propagation in viscoelastic waveguide loaded with complex fluids," *Applied Mathematical Modelling*, vol. 96, pp. 559–569, 2021.

[36] S. Nilsson, N. A. Petersson, B. Sjögreen, and H. O. Kreiss, "Stable difference approximations for the elastic wave equation in second order formulation," *SIAM Journal on Numerical Analysis*, vol. 45, no. 5, pp. 1902–1936, 2007.

[37] B. Bialecki and A. Karageorghis, "Finite difference schemes for the Cauchy–Navier equations of elasticity with variable coefficients," *Journal of Scientific Computing*, vol. 62, no. 1, pp. 78–121, 2015.

[38] B. Sjögreen and N. A. Petersson, "A fourth order accurate finite difference scheme for the elastic wave equation in second order formulation," *Journal of Scientific Computing*, vol. 52, no. 1, pp. 17–48, 2012.

[39] B. Gustafsson, *High Order Difference Methods for Time Dependent PDE*, Springer, Berlin, Germany, 2008.

[40] S. Carrino, F. Nicassio, G. Scarselli, and R. Vitolo, "Finite difference model of wave motion for structural health monitoring of single lap joints," *International Journal of Solids and Structures*, vol. 161, pp. 219–227, 2019.

[41] M. E. Gurtin, "The linear theory of elasticity," in *Linear Theories of Elasticity and Thermoelasticity*Springer, Berlin, Germany, 1973.

[42] H. P. Langtangen and S. Linge, "Finite difference computing with PDEs - a modern software approach," *Texts in Computational Science and Engineering*, vol. 23, no. 11, pp. 1219–1221, 2017.

[43] Z. Cai and S. Kim, "A finite element method using singular functions for the Poisson equation: corner singularities," *SIAM Journal on Numerical Analysis*, vol. 39, no. 1, pp. 286–299, 2001.

[44] L. Krähenbühl, F. Buret, R. Perrussel, D. Voyer, and P. Dular, "Numerical treatment of rounded and sharp corners in the modeling of 2D electrostatic fields," *Journal of Microwaves and Optoelectronics*, vol. 10, pp. 66–81, 2011.

[45] M. Dauge, S. Tordeux, and G. Vial, "Selfsimilar perturbation near a corner: matching versus multiscale expansions for a model problem," in *Around the Research of Vladimir Maz'ya II: Partial Differential Equations, International Mathematical Series*Springer, Berlin, Germany, 2010.